Journal of Materials Science & Technology 101 (2022) 95–106

Contents lists available at ScienceDirect

Journal of Materials Science & Technology

journal homepage: www.elsevier.com/locate/jmst

Research Article

Ultra-high strength yet superplasticity in a hetero-grain-sized nanocrystalline Au nanowire

Libo Fu[a], Deli Kong[a], Chengpeng Yang[a], Jiao Teng[b], Yan Lu[a], Yizhong Guo[a], Guo Yang[a], Xin Yan[c,*], Pan Liu[d], Mingwei Chen[e], Ze Zhang[f], Lihua Wang[a,*], Xiaodong Han[a,*]

[a] Beijing Key Lab of Microstructure and Properties of Advanced Materials, Beijing University of Technology, Beijing 100124, China
[b] Department of Material Physics and Chemistry, University of Science and Technology Beijing, Beijing 100083, China
[c] School of Mechanical Engineering and Automation, Beihang University, Beijing 100191, China
[d] School of Materials Science and Engineering, Shanghai Jiao Tong University, Shanghai 200240, China
[e] Department of Materials Science and Engineering, Johns Hopkins University, Baltimore, MD 21218, United States
[f] School of Materials Science and Engineering, Zhejiang University, Hangzhou 310027, China

ARTICLE INFO

Article history:
Received 20 March 2021
Revised 2 May 2021
Accepted 5 May 2021
Available online 6 August 2021

Keywords:
In situ
Mechanical property
Metallic nanowires
Transmission electron microscopy
Plastic deformation

ABSTRACT

Nanocrystalline metals often display a high strength up to the gigapascal level, yet they suffer from poor plasticity. Previous studies have shown that the development of hetero-sized grains can efficiently overcome the strength-ductility trade-off of nanocrystalline metals. However, whether this strategy can lead to the fabrication of nanocrystalline nanowires exhibiting both high strength and superplasticity is unclear, similar to the atomistic deformation mechanism. In this paper, we show that ultra-small nanocrystalline Au nanowires comprising grains in both the Hall–Petch and inverse Hall–Petch grain-size regions can exhibit extremely high uniform elongation (236%) and high strength (2.34 gigapascals) at room temperature. In situ atomic-scale observations revealed that the plastic deformation underwent two stages. In the first stage, the super-elongation ability originated from the intergrain plasticity of small grains via mechanisms such as grain boundary migration and grain rotation. This intergrain plasticity caused the grains in the heterogeneous-structured nanowires to grow very large. In the second stage, the super-elongation ability originated from intragrain plasticity accompanied by the diffusion of surface atoms. Our results show that the hetero-grain-sized nanocrystalline nanowires, comprising grains with sizes both in the strongest Hall–Petch effect region and the inverse Hall–Petch effect region, were simultaneously ultra-strong and ductile. They displayed neither a strength-ductility trade-off nor plastic instability.

1. Introduction

Metals with high ductility and strength are highly sought after owing to their various practical applications [1-3]. Revealing the atomistic deformation mechanism of metals is crucial when developing metals with a substantial improvement in both strength and ductility [2-5]. In the past decades, the atomistic deformation mechanism of nanocrystalline nanowires (NWs) has attracted a great deal of attention due to the high strength of nanocrystalline NWs compared with their bulk counterparts [5-10]. A previous study showed that nanocrystalline NWs can exhibit ultra-high strength; however, they usually exhibit a poor elongation capability [11-16]. This strength-ductility trade-off is an obstacle to their practical application [2,3,17,18]. Recently, many researchers have reported an efficient way of overcoming the strength–ductility trade-off. By developing hetero-sized grains in nanocrystalline metals, a high elongation capability was achieved [17-25]. However, whether the above-mentioned strategy is valid for nanocrystalline NWs was uncertain. Previous simulations and post-mortem experimental examinations have indicated that plasticity in large grains is governed by intragrain dislocations, while intergrain plasticity behaviors, such as grain boundary (GB) migration and grain rotation, are dominant in relatively small grains [1,4,19,26,27], which can effectively suppress strain localization and can ultimately lead to the high plastic capability of hetero-grain-sized nanocrystalline metals [1-3,18,25]. It is well established that intergrain plasticity is a high-temperature deformation mechanism that leads to the superplasticity in polycrystalline metals [28-30]. This supports the belief that once intergrain plasticity is triggered, polycrystalline metals can exhibit high plasticity or even superplasticity at room temperature. However, such high plasticity has rarely been achieved at room temperature in nanocrys-

* Corresponding authors.
E-mail addresses: yan_xin@buaa.edu.cn (X. Yan), wlh@bjut.edu.cn (L. Wang), xdhan@bjut.edu.cn (X. Han).

https://doi.org/10.1016/j.jmst.2021.05.063
1005-0302/

talline NWs. Their plasticity is dominated by intergrain plasticity [5,31,32]. Whether GB-mediated plasticity can lead to ultrahigh or even superplasticity in metallic NWs that comprise hetero-sized grains at room temperature is uncertain. To the best of our knowledge, most previous studies have been conducted on the hetero-grain-sized nanocrystalline metals [1,17,18,21,23-27]. However, hetero-grain-sized nanocrystalline NWs with a large free surface have rarely been investigated. Studies on the hetero-grain-sized nanocrystalline NW response and on the atomic-scale deformation mechanism are heavily dependent on molecular dynamics simulations because of a lack of in situ atomic-scale experimental evidence [10-13,23,26,32-35].

In this study, the deformation behavior of hetero-grain-sized nanocrystalline Au NW with a diameter of ~19 nm was studied using a homemade bimetallic extensor [36,37]. The results showed that the hetero-grain-sized nanocrystalline NW exhibited a superplasticity higher than 200% and a superior strength greater than 2.34 gigapascals at room temperature. In situ atomic-scale observation revealed that the superplastic elongation ability originated from the coordination of intergrain plasticity and intragrain dislocation. In the early deformation stage, plasticity was governed by the intergrain plasticity of the small grains, which led to the growth of large grains in heterogeneous-structured NW. Thereafter, plasticity was governed by intragrain dislocations accompanied by the diffusion of surface atoms.

2. Experimental

2.1. In situ TEM tensile deformation

The hetero-grain-sized nanocrystalline Au NWs were fabricated via NanoMill thinning. First, a nanocrystalline Au thin film with ~25 nm thick was fabricated via magnetron sputtering onto a single NaCl crystal substrate. Under an optical microscope, the thin film with the NaCl substrate was attached to a bimetallic strip extensor, followed by the removal of the NaCl substrate by etching with water. The thin film remaining on the bimetallic strip extensor was further thinned using a Fischione 1040 NanoMill. After thinning, many ligaments spanned the open void. Each ligament served as nanocrystalline Au NW. Some of these NWs displayed hetero-grain-sized structures, while other NWs displayed homogeneous grain sizes. Then, the bimetallic strip extensor was mounted in an FEI Titan G^2 (300 kV) transmission electron microscope (TEM) with a heating specimen holder at double tilt. The homemade bimetallic strip extensor [36,37] comprised two thin layers of dissimilar materials with a large mismatch in thermal expansion coefficients. This resulted in large displacements at relatively low operating temperatures (< 50°C, far below the melting point of Au, which is ~1064°C). During testing, the temperature controller accurately increased the temperature for the heating stage. Then, the bimetallic extensor exerted a tensile force on the NW to ensure slow and gentle deformation of the NW at a strain rate of $\sim 4 \times 10^{-3}$ s^{-1}. The elastic tensile strain during loading was quantified by measuring the distance of dots that obtained from fast fourier transform (FFT) of high-resolution TEM (HRTEM) images [38] (more details are found in Fig. S1 in Supplementary Material).

2.2. Atomistic modeling

We performed molecular dynamics simulations of the plastic stretching of a heterogeneous nanocrystalline Au structure using a large-scale atomic/molecular massively parallel simulator program with an embedded-atom method (EAM) potential [39,40]. A sample with a length, width, and thickness of 45 nm, 22 nm, and 3 nm, respectively, was simulated. Two half-circle notches with a radius of 42.5 nm were created, and the center of each half-circle was 38 nm from the original edge of the sample. The sample comprised 12 grains with different sizes (Fig. S2). These sizes closely matched those of grains used in the experiments. The system comprised 212869 atoms. The out-of-plane orientation of all grains was $[\bar{1}10]$. The periodic boundary condition was applied in the out-of-plane direction, while freedom was allowed in the remaining two directions. The entire system was equilibrated for 200 ps at the beginning of the simulation. After equilibration, the samples were stretched lengthwise. Step loading was adopted in this simulation [41]. For each loading step, a 5 ps equilibration period was allowed after the system was stretched for 5 ps at a strain rate of 10^8 s^{-1}. During the simulation, the temperature was maintained at 300 K using the Berendsen thermostat. The atomistic structures were visualized using Open Visualization Tool (OVITO) software [42].

3. Results

3.1. The ultra-large plasticity of the hetero-grain-sized nanocrystalline Au NW

Fig. 1 displays a series of low magnification TEM images representing the in situ observation of the tensile test of a hetero-grain-sized nanocrystalline NW. The NW exhibited ultra-high plasticity under tensile deformation. Fig. 1(a) shows a TEM image captured during the early deformation stage. The image shows a NW with a diameter of ~19 nm comprising nanograins with large size differences. G_1 and G_2, with grain sizes of 17 × 12 nm and 12 × 15 nm, respectively, fall into the Hall–Petch effect grain-size region [4,26], while G_3 and G_4, with grain sizes of 6 × 7 nm and 5 × 7 nm, respectively, fall into the inverse Hall–Petch effect grain-size region [4,26] (also refer to the statistical distribution of grain sizes in Fig. 1(g)). This structure is described as a heterogeneous polycrystalline structure. Here, a heterostructure is defined as an inhomogeneous structure that exists in various domains, each with dramatically different properties [17,18]. It can include heterogeneous grain/lamellar/phase structures, gradient structures, nanotwins, and nanoprecipitates [17,25,43,44]. Grain size is one of the most important microstructural parameters and is a key determinant of the mechanical properties of metals [2,3]. A heterogeneous grain size distribution leads to enhanced strain hardening and, consequently, uniform tensile ductility at high flow stresses [17,18,24,45]. To track the plastic strain, two regions displaying no apparent strain served as fixed references and are indicated by the red lines in the figures. The strain (ε) can be calculated using the formula: $\varepsilon = (L_n - L_0)/L_0$, where L_0 is the initial distance between the two references and L_n is the distance between the two references after deformation. As observed in Fig. 1(a–f), the NW exhibited a homogeneous tensile elongation as high as 236%. The changing microstructure of the NW in Fig. 1(a–d) shows how the sizes of G_1–G_4 changed during tensile loading. The NW contained a large grain with a size of ~28 × 12 nm^2 (i.e., nearly a single crystal). Interestingly, the diameter of the NW decreased from 19.41 nm (Fig. 1(a)) to 9.74 nm (Fig. 1(f)) during the tensile test.

The elongation strain *vs.* diameter reduction curve is shown in Fig. 1(h) (more details are found in supplementary material, Fig. S3). The blue dots represent experimental measurements. Clearly, the diameter reductions during the experiments were larger than those from the theoretical predictions of the final deformation stage. This indicates that the external decrease in diameter was due to diffusion of surface atoms. A detailed analysis showed that the grain rotation of small grains and GB migration were observed during the early deformation stage. After the grains grew into larger grains, lattice dislocations and surface atom diffusion were also observed in the nanocrystalline NW (Figs. 2-7).

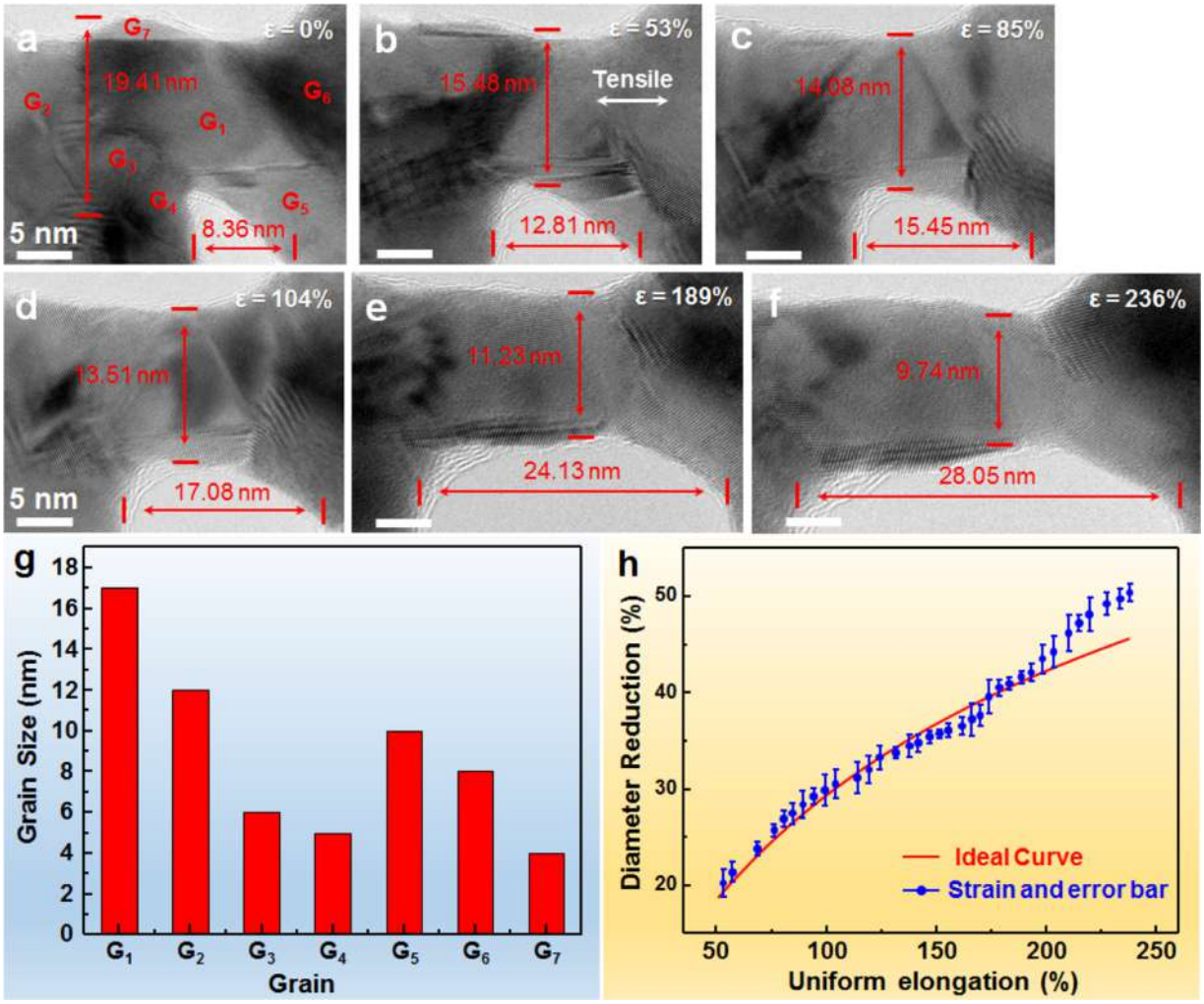

Fig. 1. Ultra-high plasticity of a hetero-grain-sized nanocrystalline Au NW. (a–f) Series of TEM images showing the tensile deformation of the Au NW. The references are indicated by short red lines. The symbol ε represents the total strain during each tensile stage. The scale bar is 5 nm. (g) Grain size distribution of the hetero-grain-sized Au NW. (h) Curve of elongation strain *vs.* diameter reduction.

3.2. Intergrain plasticity for small-sized grain in hetero-grain-sized nanocrystalline Au NW

To study the atomic-scale intergrain plasticity, Fig. 2 shows several images captured during different deformation stages. Fig. 2(a) displays the HRTEM image captured at a strain of ~4%. The loading orientation is indicated by a white arrow. When the loading increased, GB migration occurred, leading to grain growth (Fig. 2(c–f)). As the strain increased to 53% (Fig. 2(b)), the NW was transformed into a single crystal. Fig. 2(c–f) shows four enlarged HRTEM images corresponding to the white framed region in Fig. 2(a). The images show grain growth resulting from GB migration. These four images were captured as the strain increased from 4% to 53%. The time scales for (a), (b), (c), and (d) were 0 s, 22 s, 59.5 s, and 93 s, respectively. In Fig. 2(c), four grains were labeled G_1–G_4 to illustrate the GB plastic deformation process. The GB is indicated by a white dotted line. For convenience, $G_{i\text{-}j}$ is defined as the GB between grains G_i and G_j, the shape and positional change of $G_{i\text{-}j}$ during GB migration, and the misorientation angle change between two grains during grain rotation. During straining, as shown in Fig. 2(c) and (d), $G_{2\text{-}3}$ and $G_{2\text{-}4}$ exhibited visible movement, indicating that GB migration occurred during the deformation of the nanocrystalline NW. As shown in Fig. 2(d–f), with further in situ strain, the sizes of G_3 and G_4 decreased until they ultimately disappeared (additional details are found in Fig. S4), while the size of G_1 increased. This GB-mediated plasticity ultimately led to the formation of a ~28 × 12 nm^2 grain in the heterogeneously structured NW. In addition to GB migration, grain rotation was observed during deformation.

In addition to GB migration, coupled GB migration and grain rotation were frequently observed during tensile loading. In Fig. 3, another four grains, labeled G_1–G_4, can be distinguished by their different contrasts and lattice orientations. The GB is indicated by a white dotted line. As shown in Fig. 3(a), the GB angle of $G_{2\text{-}4}$ was ~9.1° during the early deformation stage. With further loading, the GB angle of $G_{2\text{-}4}$ increased from ~9.1° to ~10.5° and then to ~14.2° (Fig. 3(b) and (c)). Meanwhile, $G_{1\text{-}2}$ and $G_{1\text{-}4}$ migrated downward, resulting in a decrease in the grain sizes of G_2 and G_4. As the strain increased further, (Fig. 3(c) and (d)), $G_{3\text{-}4}$ moved toward the interior of G_4, and the size of G_4 decreased until it finally disappeared. This provided direct evidence of coupled GB migration and grain rotation during deformation. As can be observed in Fig. 3(d–f), with further loading, $G_{1\text{-}2}$ continued to move downward and $G_{1\text{-}3}$ moved downward to the right. This cooperative GB migration ultimately led to the downward migration of $G_{1\text{-}2}$ to the free surface of the NW, accompanied by a sharp decrease in the grain size of G_2. This coupled GB migration and grain rotation assisted in alleviating deformation localization and prevented plastic instability [23]. Moreover, the ductility of the nanocrystalline NW improved. Thus, coupled GB migration and grain rotation also

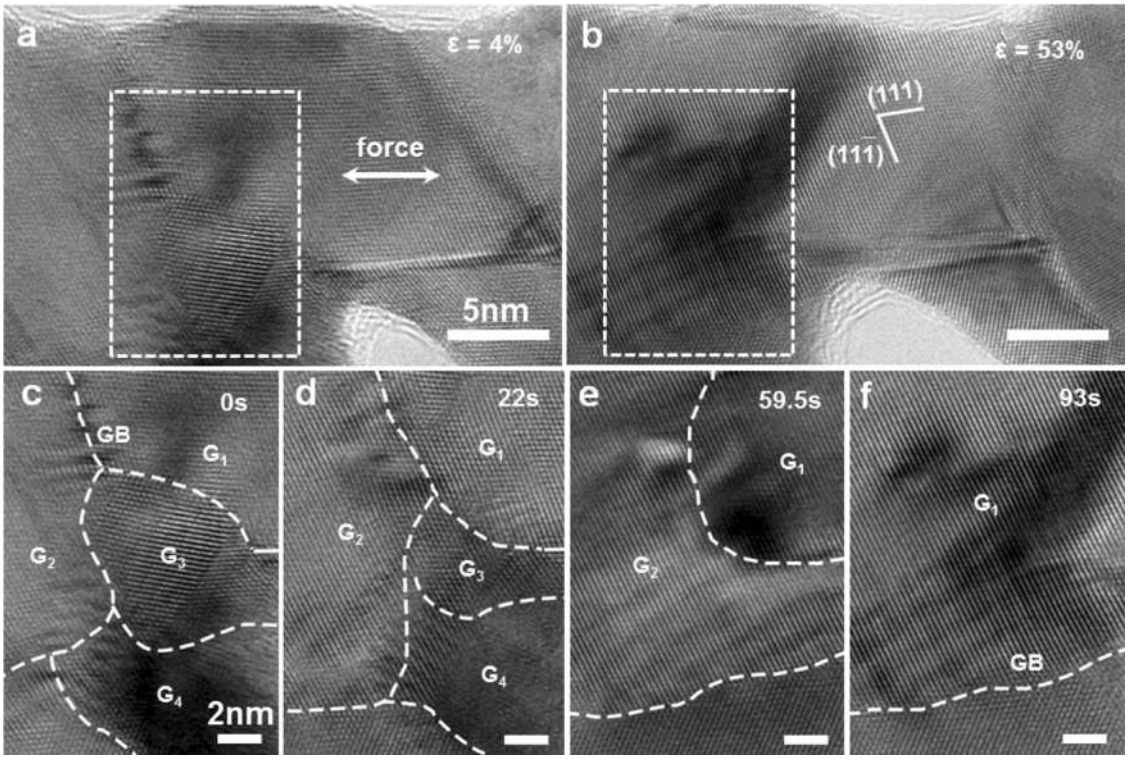

Fig. 2. GB migration-induced grain growth in a hetero-grain-sized nanocrystalline Au NW. (a, b) HRTEM images showing grain boundary plasticity leading to grain growth in the heterogeneous- structured nanocrystalline Au NW subjected to strain. The scale bar is 5nm. (c–f) Enlarged HRTEM images of the white framed regions in (a) and (b) show the GB migration and grain growth more clearly. The scale bar is 2 nm.

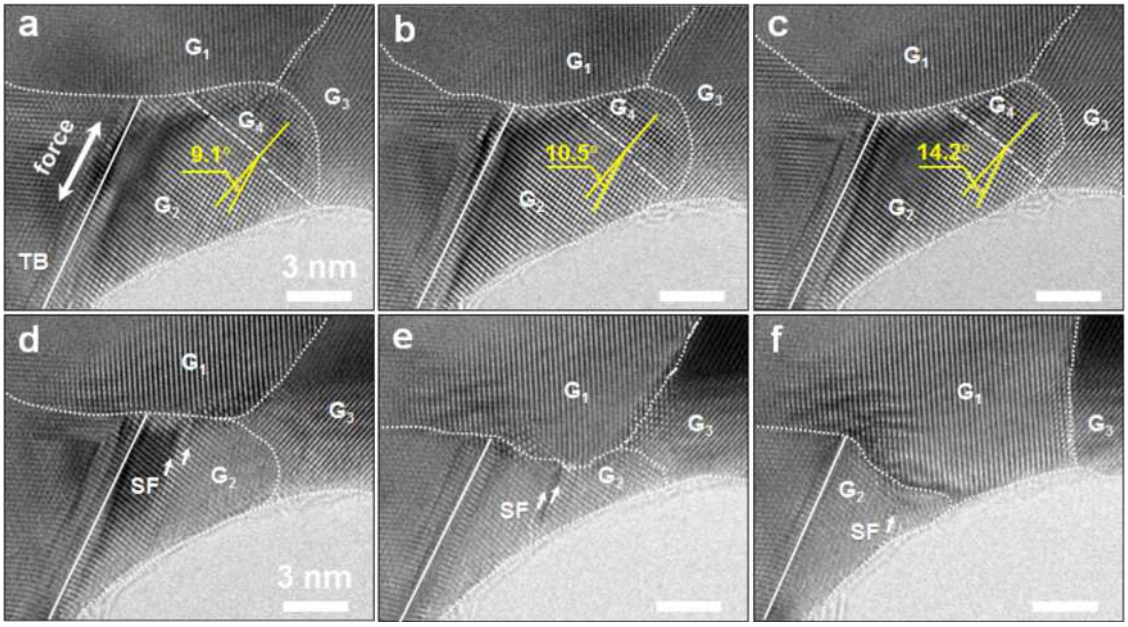

Fig. 3. (a) Four grains labeled G_1-G_4. Their GBs are indicated by a white dotted line. (b, c) With further loading, the orientation angle between G_2 and G_4 increased from ~9.1° to ~ 14.2°. Simultaneously, the GB also migrated. (d-f) Movement of the GB of $G_{1\text{-}2}$ toward the surface of the NW, GBs of $G_{2\text{-}3}$ and $G_{1\text{-}3}$ simultaneously changed dramatically.

play an important role in the superplasticity of hetero-grain-sized nanocrystalline NW.

3.3. Intragrain dislocation for large-sized grain in hetero-grain-sized nanocrystalline Au NW

During the late deformation stage, the structure of the NW was almost transformed into that of a single crystal. During this stage, dislocation activity was frequently observed. Fig. 4 displays a series of HRTEM images captured along the $[1\bar{1}0]$ axis. It shows the atomic-scale evolution of dislocations after the growth of a large grain. The deformation mechanism was governed by dislocation activities and surface diffusion (Figs. 4–7). To illustrate the dynamic process of the dislocation behavior, Fig. 4(a) represents the initial time. In Fig. 4(a), a full dislocation, D_1, with a Burgers vector of $\boldsymbol{b} = \frac{1}{2}[011]$ in the $(11\bar{1})$ plane was observed in the region

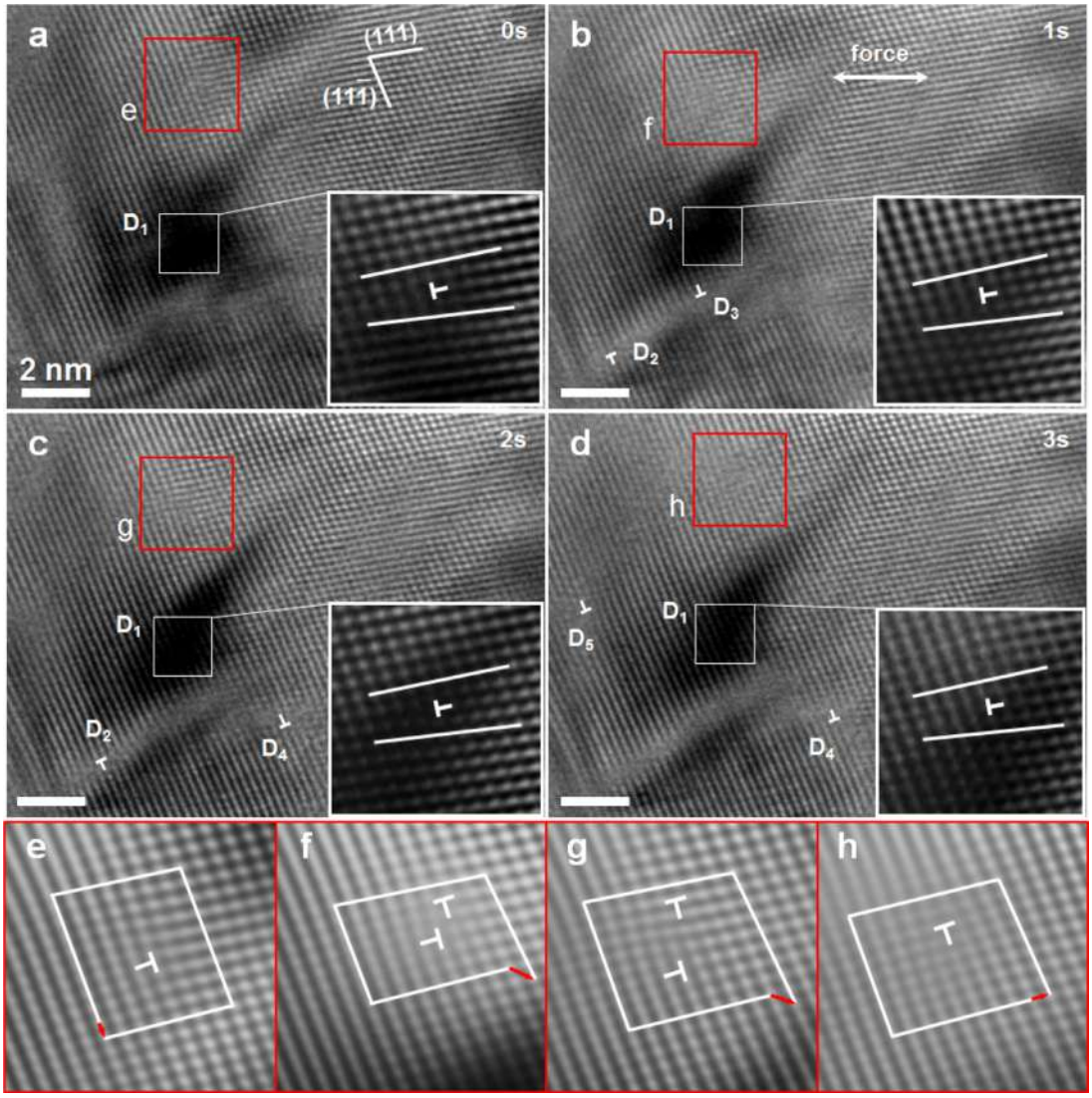

Fig. 4. In situ atomic-scale observation of full dislocation activities in a large grain. (a) Full dislocation D_1 (labeled "T") with a Burgers vector of $\boldsymbol{b} = \frac{1}{2}[011](11\bar{1})$ was observed in the large grain. (b) With continued strain, two full dislocations, D_2 and D_3, nucleated near D_1. (c) With further loading, D_3 disappeared and a new dislocation, D_4, nucleated. (d) With further loading, D_2 disappeared and a new dislocation, D_5, nucleated. (e–h) Enlarged HRTEM images corresponding to the red-framed regions in (a–d). These are in situ atomic-scale observation of the LD lock generation and destruction processes.

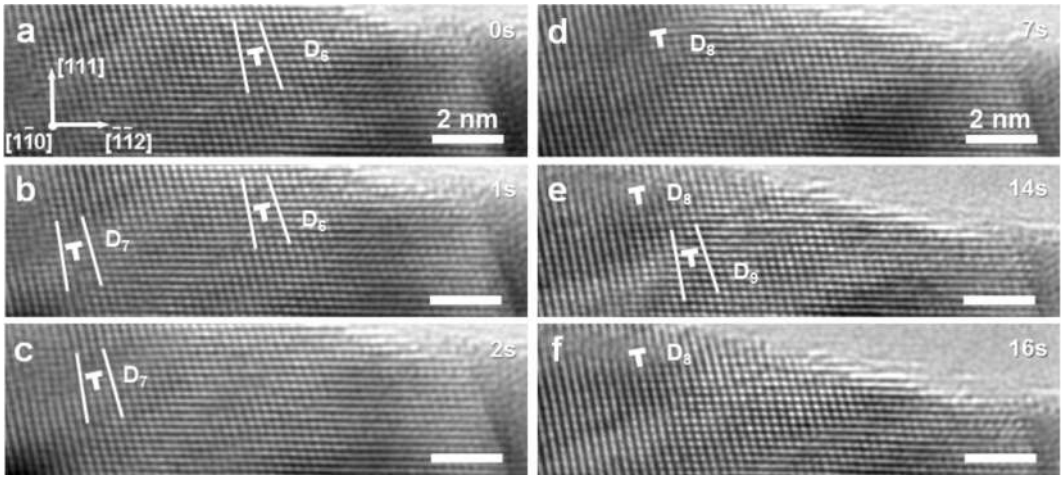

Fig. 5. In situ atomic-scale observation of full dislocation activities in a large grain near the NW surface. (a–c) Three HRTEM images captured ~1 s apart showing full dislocation activities: nucleation and a slide toward the surface. (d–f) Another typical example of dislocation. The dislocation labeled D_8 remained in the same region and another full dislocation, D_9, slipped toward the surface and disappeared.

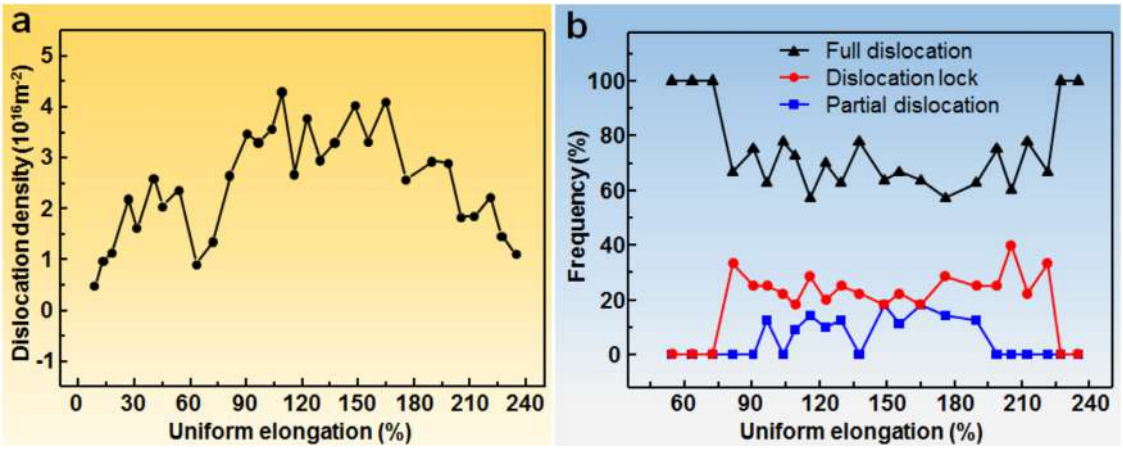

Fig. 6. (a) Statistical data of dislocation density *vs.* uniform elongation. At first, dislocation density increased as the strain increased. Then it remained high as deformation continued. (b) Statistical data show the proportion of full dislocations, partial dislocations resulting in stacking faults, and dislocation locks at different strains.

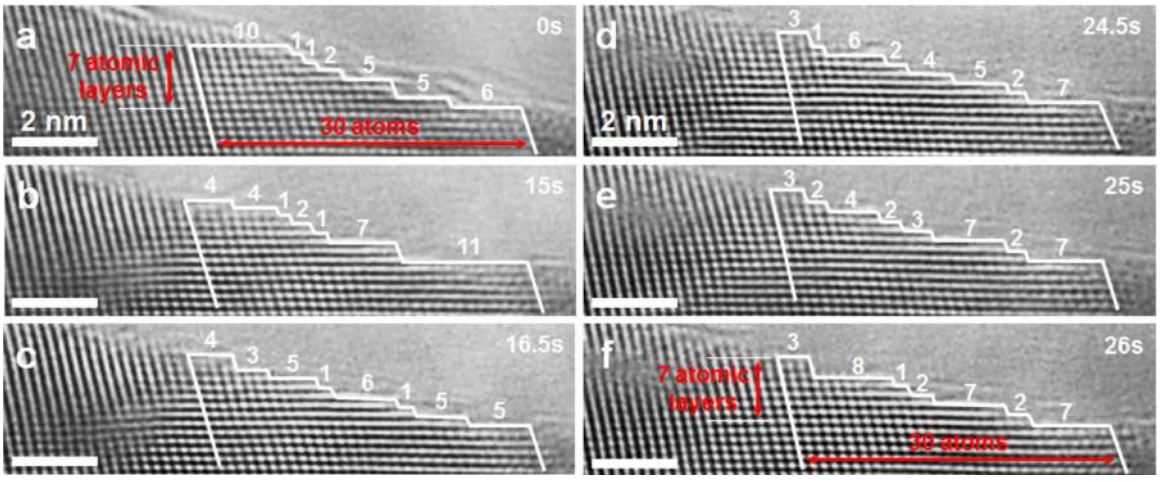

Fig. 7. In situ atomic-scale observation of surface diffusion during tensile deformation of a hetero-grain-sized NW. The surface of the NW displayed steps with different lengths and heights. The steps are indicated by the white zigzag line, and each step's length is represented numerically. During straining, diffusion of the surface atoms led to changes in the lengths and heights of the steps.

donated by "T". This dislocation remained in the same position during straining. In Fig. 4(b), two new full dislocations, D_2 and D_3, nucleated in the NW. The two dislocations were in the (111) plane with Burgers vectors of $\boldsymbol{b} = \frac{1}{2}[01\bar{1}]$ and $\boldsymbol{b} = \frac{1}{2}[10\bar{1}]$. As the strain increased (Fig. 4(c)), D_3 disappeared. With continuous loading (Fig. 4(c) and (d)), D_2 and D_4 underwent slippage, and D_2 disappeared. A new full dislocation D_5 simultaneously nucleated, as shown in Fig. 4(d). In addition to dislocation nucleation and motion, the full dislocations slip on their glide planes and reacted to form Lomer dislocation (LD) locks [36,46].

Fig. 4(e-h) shows enlarged HRTEM images corresponding to the red-framed regions of Fig. 4(a-d). The images illustrate the formation of a typical LD lock, as well as its destruction. As shown in Fig. 4(e), the Burgers circuit indicated a full dislocation with a Burgers vector of $\boldsymbol{b} = \frac{1}{2}[101]$. Further strain (Fig. 4(f)) resulted in a new type of dislocation structure. The Burgers circuit shows two extra half-planes at the crossing of the $(11\bar{1})$ and (111) planes. This represents an LD lock with $\boldsymbol{b} = \frac{1}{2}[110]$ [36,46]. The LD lock was formed by the interaction of two 60° full dislocations with Burgers vectors $\boldsymbol{b} = \frac{1}{2}[101]$ and $\boldsymbol{b} = \frac{1}{2}[01\bar{1}]$ moving under applied stress on two intersecting glide planes: $(11\bar{1})$ and (111) [36,46]. The dislocation reaction can be expressed as follows:

$$\begin{aligned} &\frac{1}{2}\left[01\bar{1}\right] + \frac{1}{2}[101] \rightarrow \frac{1}{2}[110] \\ &\text{or } \frac{1}{2}\left[10\bar{1}\right] + \frac{1}{2}[011] \rightarrow \frac{1}{2}[110] \end{aligned} \tag{1}$$

The two 60° dislocations knitted to achieve a low-energy configuration [36]. The b^2 criterion for the dislocation energy per unit length indicates a considerable energy reduction after the reaction.

With further loading, a comparison of Fig. 4(g) and (h) reveals the destruction of the LD lock at the atomic scale in which two dislocations, with Burgers vectors of $\boldsymbol{b} = \frac{1}{2}[101]$ and $\boldsymbol{b} = \frac{1}{2}[01\bar{1}]$ were quite close. After extensive straining, the dislocation with a Burgers vector of $\boldsymbol{b} = \frac{1}{2}[101]$ glided away from this region, and only one dislocation with a Burgers vector of $\boldsymbol{b} = \frac{1}{2}[01\bar{1}]$ was observed. This indicated that the LD lock was unlocked under high stress according to the following reactions:

$$\begin{aligned} &\frac{1}{2}[110] \rightarrow \frac{1}{2}\left[01\bar{1}\right] + \frac{1}{2}[101] \\ &\text{or } \frac{1}{2}[110] \rightarrow \frac{1}{2}\left[10\bar{1}\right] + \frac{1}{2}[011] \end{aligned} \tag{2}$$

Fig. 5 presents a typical example of full dislocation activities near the free surface of the NW. The double-ended arrow in Fig. 5(a) indicates the loading axis. As shown in Fig. 5(a), a full dislocation, D_6, with a Burgers vector of $\boldsymbol{b} = \frac{1}{2}[01\bar{1}]$ was observed in this region. As the strain increasing (Fig. 5(b)), a new full dislocation, D_7, was observed. With further loading (Fig. 5(c)), D_6 slipped and disappeared from the surface one second later. Thereafter, only D_7 was observed in the region. Fig. 5(d–f) displays another example of full dislocation behavior near the surface of the NW. In Fig. 5(d), a full dislocation, D_8, was generated near the surface.

This dislocation moved minimally from its original position during straining (Fig. 5(e) and (f)). As can be observed in Fig. 5(d–f), D_8 remained in the same position, and a new full dislocation caused D_9 to nucleate and slip toward the free surface before it ultimately disappeared.

To clarify the dislocation activities in the hetero-grain-sized nanocrystalline NW, Fig. 6(a) presents statistical data of dislocation density as a function of the uniform elongation of G_1 in Fig. 1. During the early stage of deformation, plastic deformation was dominated by GB plasticity, and the density of lattice dislocations was ~4.9 × 10^{15} m^{-2}, which is relatively low. As the strain increased, the density of the dislocations increased. This corresponded to the NW undergoing a transition from nanocrystals to a single crystal due to GB plasticity. During a later deformation stage, the nanocrystalline NW was transformed into a single crystal and the density of lattice dislocations remained almost constant at ~ 3.2 × 10^{16} m^{-2}. During this stage, deformation was dominated by lattice dislocations.

Fig. 6(b) presents statistical data that show the proportions of full dislocations, LD locks, and partial dislocations corresponding to tensile strains of 50–240%. Because deformation at this late stage is dominated by lattice dislocations, the proportions of these three types of dislocations can be quantified. The proportions remained almost constant during deformation. The proportion of full dislocations was always above ~80% (including both full dislocations and LD locks), while that of partial dislocations was below ~20%. This indicates that the deformation of the NW was governed by full dislocations. Additionally, we noticed that the proportion of LDs was very high. The LD lock is a source of strain hardening because high stress is required to break the lock. LD locks can also obstruct other dislocations [47,48]. The high proportion of LDs may be in the cause of the observed strain hardening in Fig. 12.

3.4. Surface diffusion in hetero-grain-sized nanocrystalline Au NW

In addition to dislocations, surface diffusion was detected during loading. Fig. 7 presents a typical example of the in-situ observation of surface diffusion at the atomic scale during deformation. To track the surface diffusion process, an unchanging position was used as a reference, as indicated by the red dashed line. As shown in Fig. 7(a), the surface of the NW displayed atomic-scale steps with different lengths and heights. The surface steps are indicated by a red zigzag line. In Fig. 7(a), six steps with a total of 7 atomic layers in height and 30 atomic layers in length were noted in the observed region. These six steps were 6, 5, 5, 2, 1, 1, and 10 atomic layers in length and 1, 2, 1, 1, 1, and 1 atomic layers in height. After 15 s, as shown in Fig. 7(b), the dimensions of the six steps changed to 11, 7, 1, 2, 1, 4, and 4 atomic layers in length and 2, 1, 1, 1, 1, and 1 atomic layers in height, respectively. This change in the surface steps was attributed to surface atom diffusion from the NW towards the substrate at both ends of the NW [8]. After 16.5 s, the original six steps were transformed into seven steps. The seven diffusion steps were 5, 5, 1, 6, 1, 5, 3, and 4 atomic layers in length and 1, 1, 1, 1, 1, 1, and 2 atomic layers in height. Surface atom diffusion resulting in a change in the surface steps occurred throughout tensile loading (Fig. 7(d–f)). This surface diffusion can efficiently eliminate full dislocations that result in surface steps. Moreover, surface diffusion can eliminate the tendency for plastic instability to ensure that the NWs exhibit super-elongation.

3.5. Molecular dynamic simulations

To further elucidate the deformation mechanism, a hetero-grain-sized nanocrystalline sample with a microstructure similar to that shown in Fig. 1(a) was reconstructed (Fig. 8). Molecular dynamics (MD) simulations were conducted on this sample using the EMA potential of Au. The multi-grain model was created based on Voronoi cells. To identify the motion of GBs during the deformation of the sample, the atoms were colored according to their centrosymmetric parameters (all the figures showing MD simulation results are colored according to centrosymmetric parameters using the same color bar shown in Fig. 8(a)). The morphology of the grains and the GBs in the sample, as shown in Fig. 8(a), shows 12 grains with different sizes: 7 × 7, 7 × 4, 6 × 4, 15 × 10, 22 × 12, 11 × 12, 6 × 2, 16 × 13, 19 × 17, 10 × 7, 4 × 12, and 13 × 11 nm^2. The statistical distribution of the initial grain sizes of the sample was nearly identical to that in our experiments.

Fig. 8(a–e) shows the MD result of the sample where the tensile strain increased from 0 to ~29.6%. As shown in Fig. 8(b–d), G_1–G_3 and G_7 disappeared (the grain sizes for G_1–G_3 and G_7 were in the inverse Hall–Petch effect region [4,26]) with increasing strain. Simultaneously, G_4 and G_5 merged into one grain with a size of ~30 × 17 nm^2. G_6 (the grain sizes for G_4–G_6 are in the strongest Hall–Petch effect region [4,26]) also grew from 11 × 12 nm to ~9 × 20 nm^2. A detailed analysis showed that these grain-size changes were due to GB plasticity, manifested as grain migration and grain rotation. Here, the homogenous strain in the MD simulation was much lower than that in in situ experiments. The difference may be due to the high strain rates inherent in MD [49-51]. The strain rate in the MD simulation was ~10^8 s^{-1}, which is much higher than that in the experiments (10^{-3} s^{-1}), leading to a significant difference in the homogenous strain [50]. Except for the strain rate, the semi-empirical atom potential and GB structure can also significantly affect the stress–strain curve in MD simulations.

Fig. 9 shows four enlarged images of GB migration in the MD simulation that corresponded to strain values of 3.5%, 4.7%, 6.9%, and 8.4%. The images more clearly show how GB migration leads to grain growth. In Fig. 9, blue represents atoms inside the grain, white represents atoms at the GB, and red represents atoms on the free surface. In Fig. 9(a), three grains were labeled as G_5, G_6, and G_9, while the GB was indicated by a yellow dotted line. During deformation, the position of $G_{6\text{-}9}$ did not change noticeably. Therefore, they could serve as reference points to track GB migration. In Fig. 9(a), the distance between $G_{6\text{-}9}$ and $G_{5\text{-}6}$ is 8 atomic layers. As the strain increased, $G_{5\text{-}6}$ moved toward the right (Fig. 9(b) and (c)), and the shape of $G_{5\text{-}6}$ visibly changed. The measured distance between $G_{6\text{-}9}$ and $G_{5\text{-}6}$ increased from the original 8 atomic layers to 17 atomic layers. With further strain (Fig. 9(d)), $G_{5\text{-}6}$ continued to move to the right, and the distance between $G_{6\text{-}9}$ and $G_{5\text{-}6}$ increased to 23 atomic layers. This is direct evidence of GB migration during the early deformation stage.

Fig. 10 shows three enlarged images of typical coupled GB migration and grain rotation processes. The corresponding strains were 0%, 2.5%, and 4.4%. The grains were labeled G_1–G_6. To track the GB movement, the GB position G_1 was indicated by a red dotted line. By comparing the GB position, grain size, and misorientation between two adjacent grains, one can observe that the GB visibly moved and that grain rotation occurred, indicating coupled GB migration and grain rotation during deformation. In Fig. 10(a), the GB angle $G_{1\text{-}4}$ was ~14°, while $G_{4\text{-}5}$ was ~16°. As the strain increased, $G_{1\text{-}2}$, $G_{1\text{-}3}$, $G_{1\text{-}4}$, and $G_{1\text{-}5}$ moved toward the interior of G_1. Additionally, as shown in Fig. 10(b) and (c), grain rotation was observed, which caused the grain boundary angles $G_{1\text{-}4}$ and $G_{4\text{-}5}$ to decrease from 14° to 8.7° and from 16° to 5.5°, respectively. During the subsequent deformation, G_1–G_4 disappeared as the strain increased further, as shown in Fig. 8(b–d). This indicated that the coupled GB migration and grain rotation played an important role in the observed superplasticity. Here, good agreement between the MD simulation and experimental observations indicated that the observed deformation mechanisms should be also valid for metallic hetero-grain-sized NWs.

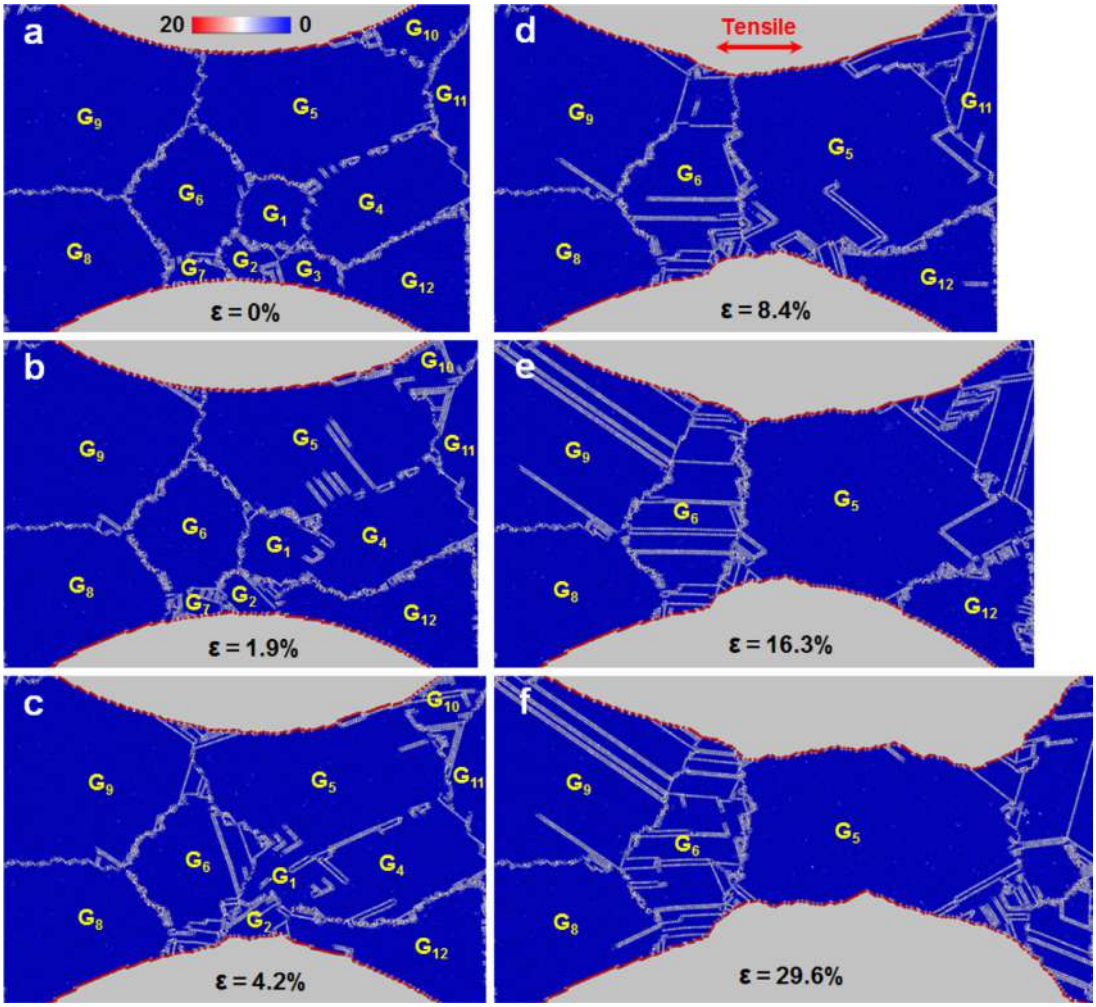

Fig. 8. Tensile deformation of a heterogeneously structured nanocrystalline Au sample in a MD simulation. MD result of the sample subjected to a tensile strain of 0 to ~29.6%. The nanocrystalline structure was subjected to tension. Small grains tended to fuse via GB plastic deformation to form large grains.

In addition to GB plasticity, surface diffusion was involved in plastic deformation in the MD simulation. Fig. 11 shows a typical example of surface diffusion during the late deformation stage. The viewing direction was along the [$\bar{1}$10], and the tensile direction was indicated by the arrow. As shown in Fig. 11(a), to track the surface diffusion process more easily, 20 consecutive atoms were highlighted in yellow. As the strain increased (Fig. 11(a) and (b)), the original yellow surface atoms were separated by red atoms. With further strain, additional red atoms were inserted between the yellow atoms, leading to a visible increase in the distances between yellow atoms. This indicates that the surface atoms diffused, causing their positions to change. In addition, as indicated by the yellow arrows in Fig. 11(b–d), several yellow atoms migrated to the lower layer, indicating that the surface atoms can diffuse in a direction perpendicular to the tensile direction. These results indicate that surface atom diffusion always occurs during deformation and can alleviate local stress and eliminate deformation localization.

3.6. The mechanical properties of the hetero-grain-sized nanocrystalline Au NW

To determine the strength (σ) and ductility (ε) of the hetero-grain-sized nanocrystalline Au NW, the elastic tensile strain along the axial <112> direction of the Au NWs during loading was quantified by measuring the distances between the dots in the FFT of HRTEM images developed by Sun et al. [38]. Here, a region on the NW after fracture served as a fixed reference for elastic strain measurements. This region was stress-free and formed approximately 90% of the NW's area; thus, it is an ideal reference region (more details are found in Fig. S5). We selected multiple positions on G_1 to measure the average elastic strain. Because the plastic deformation was homogeneous, the stress distribution was expected to be relatively homogeneous without a sudden change in stress concentration. This was confirmed by our elastic strain measurements at different positions, with values varying by ±0.05% (Fig. S5(c)). Thereafter, the stress values can be estimated using Young's modulus multiplied by the elastic strain. Here, we assumed that the Young's modulus of Au NW was constant at 78 GPa [31,52,53], as there is no reliable experimental evidence to show how size impacts Young's modulus of the NWs [54]. Further studies are needed to determine the effect of size on Young's modulus of Au and metallic nanocrystals. In Fig. 12(a), the black dotted line represents the strain and error bars measured during the experiments, while the red line is the corresponding fitted curve. The elastic strain at the first peak in the fitted curve was 3.00%, and the calculated stress was 2.34 GPa. The maximum stress in the curve was 3.56 GPa and the uniform elongation was larger than ~200%, resulting in higher values for the mechanical properties compared with those of bulk metals at room temperature. Moreover, high plasticity and superplasticity during tensile deformation at room temperature is rarely observed in nanocrystalline Au NWs or any

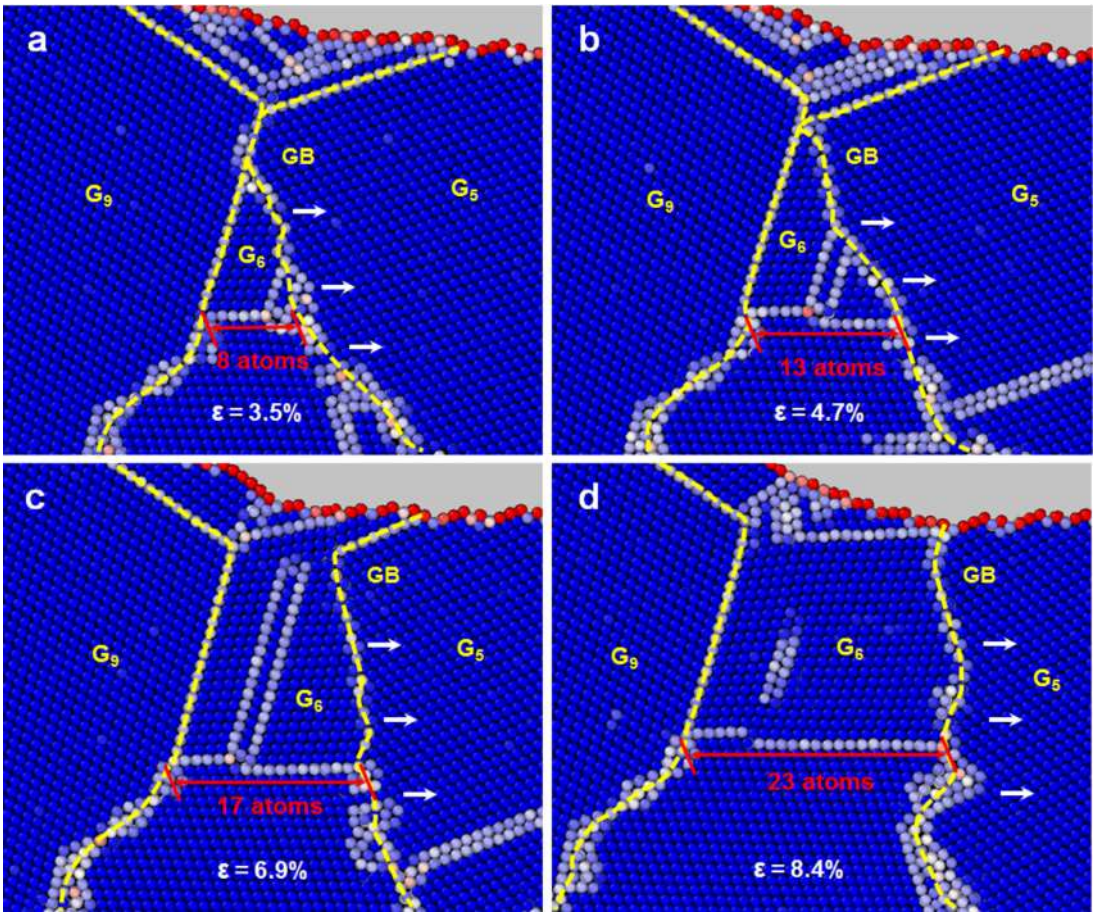

Fig. 9. Typical example of GB migration promoting grain growth in small grains in the MD simulation.

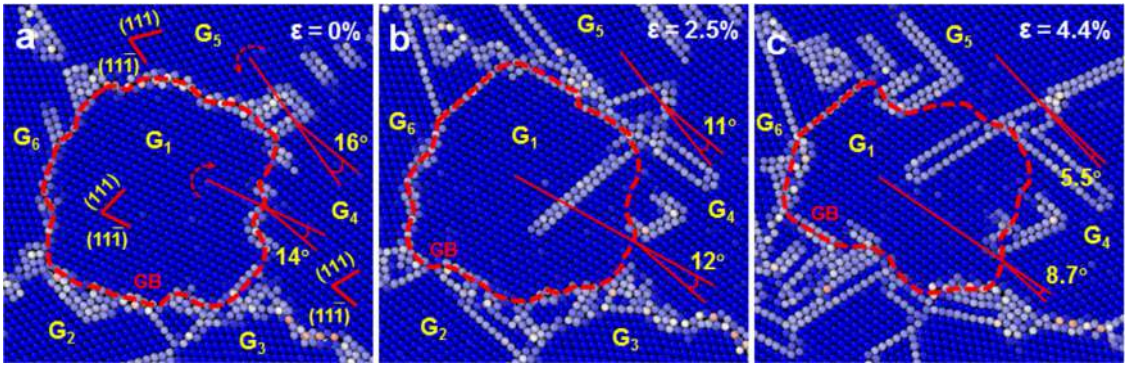

Fig. 10. Dynamic grain growth is dominated by GB migration and grain rotation. The GB position is indicated by the red dotted line. The grain boundary angles $G_{1\text{-}4}$ and $G_{4\text{-}5}$ decreased from 14° to 8.7° and from 16° to 5.5°, respectively.

other metal NWs, more examples of which are shown in Figs. S6 and S7.

To further clarify how the hetero-grain-sized nanocrystalline Au NW exhibit high strength, a statistical analysis of the mechanical properties (i.e., strength and ductility) of different metallic materials are shown in Fig. 12(b), including metallic alloys, gradient nanostructured (GNS) metals, entropy alloys, metallic single-crystal, and nanocrystalline NW [2,3,7,8,10-24,30-35,55-79]. Fig. 12(b) shows the statistical data for elongation versus the product of strength and ductility of the heterogeneous-structured nanocrystalline Au NW compared with that of other high-performance materials. Most metals and alloys exhibited a poor elongation ability, displaying a tradeoff between strength and ductility. However, the heterogeneous-structured nanocrystalline Au NWs displayed an extremely high value for $\sigma \times \varepsilon$ (~552 GPa %, based on a stress of 2.34 GPa and a strain of 236%, as shown in Fig. 12(a), indicated by a star) compared with other metals and alloys at room temperature. This demonstrates that the hetero-grain-sized nanocrystalline NWs exhibited both high strength and superplasticity and had, therefore, overcome the strength-ductility tradeoff of metallic NWs.

4. Discussion

In this study, the heterogeneously structured nanocrystalline Au NW exhibited a strength as high as 2.34 GPa and a superplastic strain of 236%. The high strength originated from the rela-

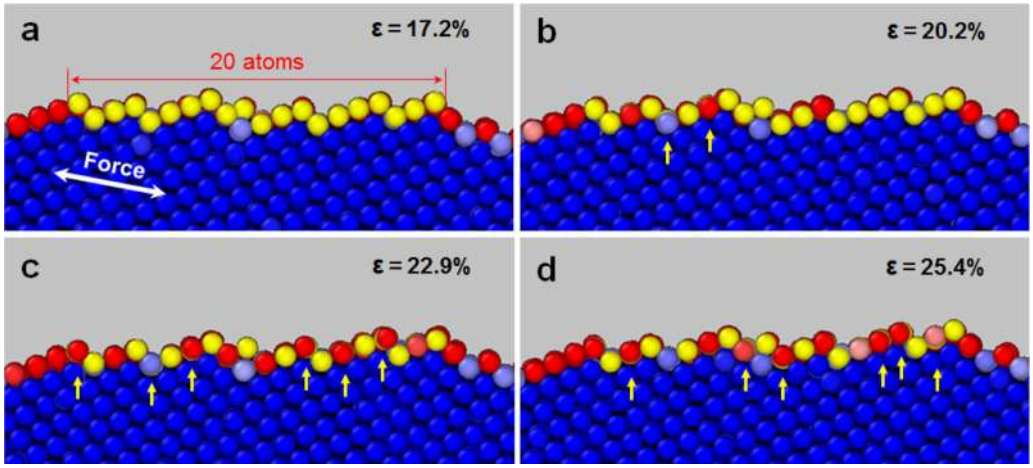

Fig. 11. Typical example showing surface diffusion both parallel to and vertical to the tensile direction.

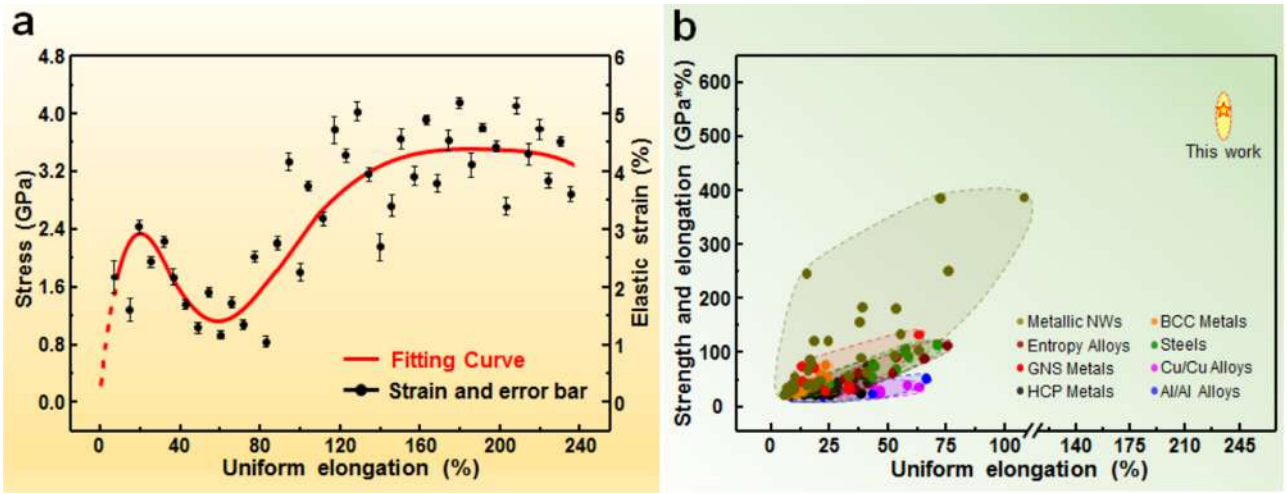

Fig. 12. (a) Statistical data for elastic strain and stress *vs.* uniform elongation. (b) Properties (elongation and the product of strength and ductility) of heterogeneously structured nanocrystalline Au NW compared with those of other high-performing materials, including different metals and alloys. The materials represented by the statistical data are divided into nine categories [2,3,7,8,10-24,30-35,55-79]: Metallic NWs (dark yellow), GNS Metals (red), Entropy Alloys (wine), BCC Metals (orange), Steels (olive), Al/Al Alloys (blue), Cu/Cu Alloys (magenta), HCP Metals (black), and This Work (stars).

tively large grains with a size of ~17 × 12 nm^2, which are in the strongest grain-size region of the Hall–Petch effect [4,26]. GB activities, dislocation activities, and surface diffusion contributed to the superplasticity. Our in situ atomic-scale observations showed that the GB activities in small grains, dislocation activities in the large grains, and surface diffusion on the NW surface contributed to the measured plasticity and that these processes could efficiently prevent local deformation instability. These results agree with previous theoretical predictions that state that a combination of dislocation and GB plasticity can lead to superplasticity [23,27-30,80,81]. This is also consistent with our MD simulation results and previous results that showed that GB plasticity occurred in nanocrystalline metals with grain sizes below ~15 nm [19,23,26,27,47,80]. Previous studies suggested that the development of heterogeneous grains in nanocrystalline metals can overcome the strength–ductility trade-off [17-25]. However, whether this strategy was valid for nanocrystalline NWs was unclear. Here, for the first time, direct atomic-scale evidence indicated that the hetero-grain-sized nanocrystalline Au NW exhibited ultra-high strength and superplasticity. Previous experiments were conducted on bulk nanocrystals rather than on NWs because nanosized NWs with hetero-grain-sized structures are difficult to fabricate [2,3,18-22,24]. In addition, most of previous studies were based on post-mortem examinations and lacked supporting in situ atomic-scale research. Therefore, it was difficult to determine the deformation mechanisms of different grain sizes in hetero-grain-sized NWs.

The ultrahigh strength and superplasticity of the hetero-grain-sized nanocrystalline Au NWs is believed to be due to the following factors: First, the hetero-grain-sized nanocrystalline Au NWs displayed a bimodal grain size distribution. The smaller grain sizes fell into the inverse Hall–Petch effect grain-size region, while the larger grain sizes fell into the Hall–Petch effect grain-size region. During early deformation, both GB plasticity in smaller grains and intragranular dislocation behavior in larger grains occurred [17,18,23,80,82]. This cooperative deformation improved the ductility of the NWs. Second, during a later deformation stage, a high density of dislocations accumulated in the NW, thereby increasing the frequency of dislocation interactions in the NW. This led to strong strain hardening that allowed the NW to undergo homogeneous plastic deformation [50,51,83,84]. Third, the size effect also significantly impacted the rate of surface atoms diffusion [5,8,13,49]. As the diameter of the NWs decreased below a critical size, the surface tension may have caused rapid diffusion of the atoms [5]. Surface atom diffusion can efficiently eliminate surface steps resulting from dislocation activities [5,8,60,85,86]. This in turn prevents step formation and stress concentration which

ensures the super-elongation ability of the NW. Previous studies have shown that high plastic deformation can be achieved when the crystal thinning rates, resulting from surface diffusion and from surface dislocation nucleation, are equal [5]. Thus, the GB plasticity and the cooperation of dislocation activities and surface atom diffusion not only contributed to high plasticity but also prevented stress concentration, which in turn enhanced strain hardening. Fourth, the initial short length of the hetero-grain-sized nanocrystalline NWs in our study many have enhanced their ductility. As suggested in previous MD simulations, metallic NWs with short lengths exhibit ductile failure, while brittle/localized shear failure often occurs as the NW length increases [13,58]. Our observed deformation mechanism differed from that in conventional metallic NWs in which dislocation activity often led to local strain concentration and early necking [9,10,24,81]. For example, previous studies showed that single crystalline or twinned NWs often fractured at a strain below 20%. In these NWs, surface atom diffusion and cooperative GB plasticity and intragranular dislocation activities were always absent. This led to their relatively low ductility. We propose that the abovementioned four factors together contributed to the superplasticity of the hetero-grain-sized Au NWs and may also be valid for other metallic or alloy hetero-grain-sized nanocrystalline NWs.

5. Conclusion

In summary, using a homemade device, tensile tests were conducted on hetero-grain-sized nanocrystalline NWs. Our results showed that the heterogeneously structured nanocrystalline NW, comprising grains with sizes in both in the strongest Hall–Petch effect region and the inverse Hall-Petch effect region, were simultaneously ultra-strong and ductile and displayed no strength-ductility trade-off nor plastic instability. In situ atomic-scale observations revealed that the superplasticity of the NWs was realized through the synergistic action of grain grown due to GB plasticity during early deformation, followed by dislocation slip accompanied by surface diffusion. These experimental findings provide a strategy for designing metals with both high strength and superplasticity.

Declaration of Competing Interest

The authors declare that they have no known competing financial interests or personal relationships that could have appeared to influence the work reported in this paper.

Acknowledgements

This work was financially supported by the Beijing Natural Science Foundation (No. Z180014) and the National Natural Foundation of China (No. 11902014). The simulation is carried out with the support of Information Office of Beihang University for the supply of High Performance Computing Platform.

Supplementary materials

Supplementary material associated with this article can be found, in the online version, at doi:10.1016/j.jmst.2021.05.063.

References

[1] S. Yip, Nature 391 (1998) 532–533.
[2] I.A. Ovid'ko, R.Z. Valiev, Y.T. Zhu, Prog. Mater. Sci. 94 (2018) 462–540.
[3] Y. Cao, S. Ni, X.Z. Liao, M. Song, Y.T. Zhu, Mater. Sci. Eng. R 133 (2018) 1–59.
[4] Q. Zhu, G. Cao, J.W. Wang, C. Deng, J.X. Li, Z. Zhang, S.X. Mao, Nat. Commun. 10 (2019) 156.
[5] L. Zhong, F. Sansoz, Y. He, C. Wang, Z. Zhang, S.X. Mao, Nat. Mater. 16 (2017) 439–445.
[6] S.C. Zhao, Q. Zhu, X.H. An, H. Wei, K.X. Song, S.X. Mao, J.W. Wang, J. Mater. Sci. Technol. 53 (2020) 118–125.
[7] S.J. Hao, L.S. Cui, D.Q. Jiang, X.D. Han, Y. Ren, J. Jiang, Y.N. Liu, Z.Y. Liu, S.C. Mao, Y.D. Wang, Y. Li, X.B. Ren, X.D. Ding, S. Wang, C. Yu, X.B. Shi, M.S. Du, F. Yang, Y.J. Zheng, Z. Zhang, X.D. Li, D.E. Brown, J. Li, Science 339 (2013) 1191–1194.
[8] S.D. Sun, D.L. Kong, D.H. Li, X.Z. Liao, D.M. Liu, S. Mao, Z. Zhang, L.H. Wang, X.D. Han, ACS Nano 13 (2019) 8708–8716.
[9] H. Zheng, A.J. Cao, C.R. Weinberger, J.Y. Huang, K. Du, J.B. Wang, Y.Y. Ma, Y.N. Xia, S.X. Mao, Nat. Commun. 1 (2010) 144.
[10] Y. Lu, J. Song, J.Y. Huang, J. Lou, Adv. Funct. Mater. 21 (2011) 3982–3989.
[11] J.W. Wang, Z. Zeng, C.R. Weinberger, Z. Zhang, T. Zhu, S.X. Mao, Nat. Mater. 14 (2015) 594–600.
[12] C. Deng, F. Sansoz, ACS Nano 3 (2009) 3001–3008.
[13] Z.X. Wu, Y.W. Zhang, M.H. Jhon, J.R. Greer, D.J. Srolovitz, Acta Mater. 61 (2013) 1831–1842.
[14] Y. Lu, C. Peng, Y. Ganesan, J.Y. Huang, J. Lou, Nanotechnology 22 (2011) 355702.
[15] C. Deng, F. Sansoz, Nano Lett. 9 (2009) 1517–1522.
[16] K. Cao, Y. Han, H. Zhang, L. Gao, Y. Lu, Nanotechnology 29 (2018) 295703.
[17] Y.T. Zhu, K. Ameyama, P.M. Anderson, I.J. Beyerlein, H.J. Gao, H.S. Kim, E. Lavernia, S. Mathaudhu, H. Mughrabi, R.O. Ritchie, N. Tsuji, X.Y. Zhang, X.L. Wu, Mater. Res. Lett. 9 (2021) 1–31.
[18] E. Ma, T. Zhu, Mater. Today 20 (2017) 323–331.
[19] J.R. Greer, J.T.M. De Hosson, Prog. Mater. Sci. 56 (2011) 654–724.
[20] X.L. Wu, P. Jiang, L. Chen, F.P. Yuan, Y.T. Zhu, Proc. Natl. Acad. Sci. USA 111 (2014) 7197–7201.
[21] Y. Wei, Y. Li, L. Zhu, Y. Liu, X. Lei, G. Wang, Y. Wu, Z. Mi, J. Liu, H. Wang, H. Gao, Nat. Commun. 5 (2014) 3580.
[22] T.H. Fang, W.L. Li, N.R. Tao, K. Lu, Science 331 (2011) 1587–1590.
[23] P.H. Cao, Nano Lett. 20 (2020) 1440–1446.
[24] Z. Cheng, H.F. Zhou, Q.H. Lu, H.J. Gao, L. Lu, Science 362 (2018) 559–567.
[25] K. Lu, Science 345 (2014) 1455–1456.
[26] J. Schiotz, K.W. Jacobson, Science 301 (2003) 1357–1359.
[27] T.J. Rupert, D.S. Gianola, Y. Gan, K.J. Hemker, Science 326 (2009) 1686–1690.
[28] P. Hidalgo-Manrique, A. Orozco-Caballero, C.M. Cepeda-Jiménez, O.A. Ruano, F. Carreño, J. Mater. Sci. Technol. 32 (2016) 774–782.
[29] H. Masuda, T. Kanazawa, H. Tobe, E. Sato, Scr. Mater. 149 (2018) 84–87.
[30] J.W. Liang, Y.F. Shen, R.D.K. Misra, P.K. Liaw, J. Mater. Sci. Technol. 83 (2021) 131–144.
[31] J.H. Seo, Y. Yoo, N.Y. Park, S.W. Yoon, H. Lee, S. Han, S.W. Lee, T.Y. Seong, S.C. Lee, K. Lee, P.R. Cha, H.S. Park, B. Kim, J.P. Ahn, Nano Lett. 11 (2011) 3499–3502.
[32] D.C. Jang, X.Y. Li, H.J. Gao, J.R. Greer, Nat. Nanotechnology 7 (2012) 594–601.
[33] F. Sansoz, V. Dupont, Scr. Mater. 63 (2010) 1136–1139.
[34] Y. Zhu, Z. Li, M. Huang, Scr. Mater. 68 (2013) 663–666.
[35] W.W. Tao, P.K. Cao, H.S. Park, Nano Lett. 18 (2018) 1296–1304.
[36] L.H. Wang, J. Teng, X.C. Sha, J. Zou, Z. Zhang, X.D. Han, Nano Lett 17 (2017) 4733–4739.
[37] D. Li, X. Shu, D. Kong, H. Zhou, Y. Chen, J. Mater. Sci. Technol. 34 (2018) 2027–2034.
[38] L. Sun, F. Banhart, A.V. Krasheninnikov, J.A. Rodríguez-Manzo, M. Terrones, P.M. Ajayan, Science 312 (2006) 1199–1202.
[39] S. Plimpton, J. Comput. Phys. 117 (1995) 1–19.
[40] G. Grochola, S.P. Russo, I.K. Snook, J. Chem. Phys. 123 (2005) 204719.
[41] X. Li, Y. Wei, W. Yang, H. Gao, Proc. Natl. Acad. Sci. USA 106 (2009) 16108–16113.
[42] A. Stukowski, Model. Simul. Mater. Sci. Eng. 18 (2010) 1.
[43] Z.Q. Fu, L. Jiang, J.L. Wardini, B.E. Macdonald, H.M. Wen, W. Xiong, D.L. Zhang, Y.Z. Zhou, T.J. Rupert, W.P. Chen, E.J. Lavernia, Sci. Adv. 4 (2018) eaat8712.
[44] Y. Zhang, N.R. Tao, K. Lu, Acta Mater. 59 (2011) 6048–6058.
[45] B. Chen, J.N. Hu, Y.Q. Wang, S.Y. Zhang, S.V. Petegem, A.C.F. Cocks, D.J. Smith, P.E.J. Flewitt, Acta Mater. 85 (2015) 229–242.
[46] J.P. Hirth, J. Lothe, Theory of Dislocations, 2nd ed., Krieger Publishing, Malabar, UK, 1992.
[47] L. Wang, X. Han, P. Liu, Y. Yue, E. Ma, Phys. Rev. Lett. 105 (2010) 135501.
[48] R. Yuan, I.J. Beyerlein, C. Zhou, Acta Mater. 90 (2015) 169–181.
[49] C.R. Weinberger, W. Cai, Proc. Natl. Acad. Sci. USA 105 (2008) 14304–14307.
[50] C.Z. Zhou, I.J. Beyerlein, R. Lesar, Acta Mater. 59 (2011) 7673–7682.
[51] M. Yaghoobi, G.Z. Voyiadjis, Acta Mater. 121 (2016) 190–201.
[52] W.D. Nix, Metall. Trans. A 20 (1989) 2217–2245.
[53] H.D. Espinosa, B.C. Prorok, B. Peng, J. Mech. Phys. Solids 52 (2004) 667–689.
[54] Y.J. Chen, Q. Gao, Y.B. Wang, X.H. An, X.Z. Liao, Y.W. Mai, H.H. Tan, J. Zou, S.P. Ringer, C. Jagadish, Nano Lett. 15 (2015) 5279–5283.
[55] K. Aaron, B. Thorsten, K. Tobias, P. Robby, Acta Mater. 92 (2015) 299–308.
[56] J.W. Wang, F. Sansoz, C. Deng, G. Xu, G.R. Han, S.X. Mao, Nano Lett. 15 (2015) 3865–3870.
[57] C. Ni, Q. Zhu, J. Wang, Mater. Sci. Eng. A 733 (2018) 164–169.
[58] Z. Wu, Y.W. Zhang, M.H. Jhon, H.J. Gao, D.J. Srolovitz, Nano Lett. 12 (2012) 910–914.
[59] J.Y. Wu, S. Nagao, J.Y. He, Z.L. Zhang, Nano Lett 11 (2011) 5264–5273.
[60] G. Cao, J.W. Wang, K. Du, X.L. Wang, J.X. Li, Z. Zhang, S.X. Mao, Adv. Funct. Mater. 28 (2018) 1805258.
[61] Y.H. Wen, Z.Z. Zhu, G.F. Shao, R.Z. Zhu, Phys. E 27 (2005) 113–120.
[62] S. Saha, M.A. Motalab, M. Mahboob, Comput. Mater. Sci. 136 (2017) 52–59.
[63] S.H. Jiang, H. Wang, Y. Wu, X.J. Liu, H.H. Chen, M.J. Yao, B. Gault, D. Ponge, D. Raabe, A. Hirata, M.W. Chen, Y.D. Wang, Z.P. Lu, Nature 544 (2017) 460–464.
[64] Y. Lu, J. Song, J.Y. Huang, J. Lou, Nano Res. 4 (2011) 1261–1267.

[65] C. Peng, Y. Zhong, Y. Lu, S. Narayanan, T. Zhu, J. Lou, App. Phys. Lett. 102 (2013) 083102.
[66] Z. Liu, L. Cui, Y. Liu, D. Jiang, J. Jiang, Scr. Mater. 77 (2014) 75–78.
[67] S. Yin, G. Cheng, G. Richter, H. Gao, Y. Zhu, ACS Nano 13 (2019) 9082–9090.
[68] S. Wang, Z. Shan, H. Huang, Adv. Sci. 4 (2017) 1600332.
[69] W. Tao, P. Cao, H.S. Park, ACS Nano 12 (2018) 4984–4992.
[70] T. Yang, Y.L. Zhao, Y. Tong, Z.B. Jiao, J. Wei, J.X. Cai, X.D. Han, D. Chen, A. Hu, J.J. Kai, K. Lu, Y. Liu, C.T. Liu, Science 362 (2018) 933–937.
[71] C.M. Cepeda-Jiménez, M.T. Pérez-Prado, Acta Mater. 108 (2016) 304–316.
[72] G. Singh, U. Ramamurty, Prog. Mater. Sci. 111 (2020) 100653.
[73] L. Li, Q.H. Fang, J. Li, H. Wu, J. Alloys Compd. 775 (2019) 270–280.
[74] J.W. Bae, J.B. Seol, J. Moon, S.S. Sohn, M.J. Jang, H.Y. Um, B.J. Lee, H.S. Kim, Acta Mater. 161 (2018) 388–399.
[75] X.C. Lu, F. Roters, G.Z. Kang, D. Raabe, Int. J. Plast. 113 (2019) 52–73.
[76] H.X. Jin, J.Q. Zhou, Y.Q. Chen, Mater. Sci. Eng. A 725 (2018) 1–7.
[77] G.H. Zhao, X. Xu, D. Dye, E.J.R. Pedro, Acta Mater. 183 (2020) 155–164.
[78] J.J. Wang, N.R. Tao, Scr. Mater. 149 (2018) 16–20.
[79] Z.F. Lei, X.J. Liu, Y. Wu, H. Wang, S.H. Jiang, S.D. Wang, X.D. Hui, Y.D. Wu, B. Gault, P. Kontis, D. Raabe, L. Gu, Q.H. Zhang, H.W. Chen, H.T. Wang, J.B. Liu, K. An, Q.S. Zeng, T.G. Nieh, Z.P. Lu, Nature 563 (2018) 546–550.
[80] X. Zhou, X.Y. Li, K. Lu, Phys. Rev. Lett. 122 (2019) 126101.
[81] Y.T. Zhu, X.L. Wu, Mater. Today Nano 2 (2018) 15–20.
[82] C.H. Liu, W.J. Lu, G.J. Weng, J.J. Li, Mater. Sci. Eng. A 756 (2019) 284–290.
[83] U.F. Kocks, H. Mecking, Prog. Mater. Sci. 48 (2003) 171–273.
[84] P. Shanthraj, M.A. Zikry, Acta Mater. 59 (2011) 7695–7702.
[85] S.Y. Kim, I.H. Lee, S. Jun, Phys. Rev. B 76 (2007) 245407.
[86] S.Y. Kim, I.H. Lee, S. Jun, Phys. Rev. B 76 (2007) 245408.